Article:

Davies, CJ and Constable, CG (2014) Insights from geodynamo simulations into long-term geomagnetic field behaviour. Earth and Planetary Science Letters, 404. 238 - 249. ISSN 0012-821X

https://doi.org/10.1016/j.epsl.2014.07.042

Insights from geodynamo simulations into long-term geomagnetic field behaviour

Christopher J. Davies[a,b], Catherine G. Constable[b]

[a] *School of Earth and Environment, University of Leeds, Leeds LS2 9JT, UK (tel: +44 (0) 11 33 43 55 43; email: c.davies@leeds.ac.uk*

[b] *Institute of Geophysics and Planetary Physics, Scripps Institution of Oceanography, University of California at San Diego, La Jolla, CA, 92092-0225, USA*

Abstract

Detailed knowledge of the long-term spatial configuration and temporal variability of the geomagnetic field is lacking because of insufficient data for times prior to 10 ka. We use realisations from suitable numerical simulations to investigate three important questions about stability of the geodynamo process: is the present field representative of the past field; does a time-averaged field actually exist; and, supposing it exists, how long is needed to define such a field. Numerical geodynamo simulations are initially selected to meet existing criteria for morphological similarity to the observed magnetic field. A further criterion is introduced to evaluate similarity of long-term temporal variations. Allowing for reasonable uncertainties in the observations, observed and synthetic axial dipole moment frequency spectra for time series of order a million years in length should be fit by the same power law model. This leads us to identify diffusion time as the appropriate time scaling for such comparisons. In almost all simulations, intervals considered to have good morphological agreement between synthetic and observed field are shorter than those of poor agreement. The time needed to obtain a converged estimate of the time-averaged field was found to be comparable to the length of the simulation, even in non-reversing models, suggesting that periods of stable polarity spanning many magnetic diffusion times are needed to obtain robust estimates of the mean dipole field. Long term field variations are almost entirely attributable to the axial dipole; non-zonal components converge to long-term average values on relatively short timescales ($15-20$ kyr). In all simulations, the time-averaged spatial power spectrum is characterised by a zigzag pattern as a function of spherical harmonic degree, with relatively higher power in odd degrees than in even degrees. We suggest that long-term spatial characteristics of the observed field may emerge on averaging times that are within reach for the next generation of global time-varying paleomagnetic field models.

Keywords: Geodynamo models, Secular variation, Geomagnetic frequency spectrum, Earth's core

1. Introduction

Earth's magnetic field of internal origin displays temporal variations spanning a vast range of frequencies (Constable and Johnson, 2005; Korte and Constable, 2006). The field can change quickly as evidenced by so-called geomagnetic jerks, abrupt changes manifest on <1 year timescales (Malin and Hodder, 1982; Alexandrescu et al., 1995), and the more moderate but still rather rapid archaeomagnetic jerks seen on centennial timescales (Gallet et al., 2009). Larger changes associated with geomagnetic excursions and polarity reversals generally occur a few times every million years (Cande and Kent, 1992, 1995; Glatzmaier and Coe, 2007), but the time taken for such changes (hundreds to thousands of years) remain a matter of some debate. Global time-dependent models of the magnetic field at the core-mantle boundary (CMB) now span the past 10 yrs (e.g. Olsen et al., 2010), 400 yrs (Jackson et al., 2000), 3 kyrs (Korte and Constable, 2011), 7 kyrs (Korte and Constable, 2005), and 10 kyrs (Korte et al., 2011) and display common features such as a predominantly dipolar field, weak flux near the geographic poles, and intense patches of magnetic flux at high latitudes. These models have enabled significant advances in understanding the geodynamo process.

On timescales longer than 10 kyr there are not yet any time-varying global models of the same quality as for the Holocene time interval, although there is some progress in this area. High-quality data have generally been confined to the dipole moment (Valet et al., 2005; Ziegler et al., 2011), with time-series spanning the past 2 Myr, and detailed well-dated directional data at a few sparse locations such as Hawaii and Réunion Island (e.g. Laj et al., 2011); for the longest periods, only the geomagnetic polarity timescale (Cande and Kent, 1992, 1995) is well documented. As a consequence, fundamental questions about the long-term behaviour of the geomagnetic field remain unanswered. For example, it is not yet known if the modern field is representative of the past field, which is important for elucidating the role of external forcings on the geodynamo (Biggin et al., 2012), or how the field structure changes as it is averaged over successively longer periods. Does a time-averaged field exist, such that when averaged over sufficient time there are no significant changes upon further temporal averaging? If so, what is the structure of this field and what averaging time is needed to attain this state? Additional information is needed to answer these questions. This paper explores them using numerical geodynamo simulations and comparisons with available paleofield models.

We consider geodynamo simulations as useful tools for investigating long-term field behaviour for three reasons. Firstly, they have recovered prominent features of the modern and paleomagnetic fields (e.g. Olson and Christensen, 2002; Coe and Glatzmaier, 2006; Gubbins et al., 2007; Bloxham, 2000; Christensen and Olson, 2003; McMillan et al., 2001; Davies et al., 2008). Secondly, they provide a global representation of the magnetic field at each time point, achieving a spatial resolution that is much higher than in observational field models. Finally, high resolution simulations can be run on long timescales, providing a detailed picture of long-term processes. However, simulations cannot yet be run with the rapid rotation rates and low diffusivities associated with Earth's core, and reaching this goal in the near future seems unlikely (Glatzmaier, 2002; Davies et al., 2011). These parameters determine the balance of forces, affecting the dynamics in the simulation and the spatio-temporal characteristics of the generated magnetic fields. Indeed, a variety of field morphologies have been obtained (Kutzner and Christensen, 2002; Olson and Christensen, 2006), which raises the question of how to decide if a given simulation exhibits "Earth-like" behaviour.

Previous studies have quantified the level of agreement between synthetic and observed fields using measures based on properties of the observed field (Dormy et al., 2000; Kono and Roberts, 2002). Christensen et al. (2010) made significant progress in this regard by defining "Earth-like" behaviour based on four quantities, derived from global field models, that characterise the spatial structure of the field. The defined criteria require that the misfits between synthetic and observed values of the four quantities fall below given tolerances; a simulation that meets the criteria is considered to be morphologically similar to the observed field. We use these definitions to select dynamo simulations that are suitable for further study.

For the long (> 10 kyr) timescales of interest in this paper we require one further criterion that measures the agreement between temporal variations in synthetic and observed fields. We use the axial dipole moment as a measure of global changes in the field and do not include further complexities. Several time-dependent models are available (Constable and Johnson, 2005; Valet et al., 2005; Ziegler et al., 2011), but we focus on the more recent 2 Myr model PADM2M of (Ziegler et al., 2011). Ziegler et al. (2011) have already established that the power spectral density for

PADM2M is compatible with that from Sint-2000 (Valet et al., 2005), and Ziegler and Constable (2011) indicate that the spectrum falls off at a rate of about $f^{-7/3}$, where f is frequency, for PADM2M above a corner frequency of about 10 Myr^{-1} in agreement with falloff rate observed in some dynamo simulations. We build a power law fit to the frequency spectrum of PADM2M and require that observed and synthetic axial dipole moment spectra can be fit by the same power law model, within appropriate uncertainty levels for the observations. Simulations that meet this criterion are considered to exhibit temporal variations similar to the PADM2M model.

This paper is organised as follows. In §2 we describe the observational and numerical models used in this study. In §3 we first discuss the problem of scaling dimensionless model time into dimensional units and select two plausible time scalings based on intrinsic timescales of the magnetic field. We then compare morphological properties of the simulations with global field models using the criteria of Christensen et al. (2010)in §3.1, and temporal variations exhibited by the simulations with the observed axial dipole moment variation in §3.2. In §4 we use simulations that meet all criteria to investigate the length of time required to obtain the mean observed and synthetic axial dipole fields. We also investigate how the synthetic fields change when averaged over successively longer periods. Discussion and conclusions are presented in §5.

2. Models

2.1. Global Field Models

We use three time varying representations of the geomagnetic field: the 400 yr historical model gufm1 (Jackson et al., 2000), the 3 kyr model CALS3k.4b (Korte and

Constable, 2011), and the 2 Myr model for axial dipole moment variations PADM2M (Ziegler et al., 2011). gufm1 and CALS3k.4b are constructed by expanding the spatial dependence of the magnetic field $\mathbf{B}$ in spherical harmonics and the temporal dependence of $\mathbf{B}$ in cubic B-splines. These models are regularised in space and time and for the most recent portion of CALS3k.4b departures from the gufm1 model are penalised. It should be noted that the quality of the paleomagnetic models derived for millennial time scales is vastly inferior to that of gufm1. This is a direct consequence of poor data coverage in the southern hemisphere, and lower accuracy in the data. Detailed descriptions of the methods and inversion strategy used to construct the global models are given in Bloxham and Jackson (1992); Jackson et al. (2000); Korte and Constable (2003, 2008, 2011); Constable (2011). For longer time periods we use PADM2M which again uses cubic B-splines for temporal dependence but only aims to model variations in axial dipole moment. A complete description of PADM2M is given in Ziegler et al. (2011).

2.2. Geodynamo Models

The model setup and solution method for our convection-driven dynamo models is standard and only a brief description is given here. An incompressible, electrically conducting Boussinesq fluid with constant thermal diffusivity κ, constant coefficient of thermal expansion α, constant viscosity ν, and constant magnetic diffusivity η is contained in a spherical shell of thickness $d = r_\mathrm{o} - r_\mathrm{i}$ and aspect ratio $r_\mathrm{i}/r_\mathrm{o} = 0.35$ rotating at a rate Ω. Here, r_i corresponds to the inner boundary and r_o to the outer boundary. The nondimensional parameters are the Ekman number E, the Prandtl number Pr, the magnetic Prandtl number Pm, and the Rayleigh number Ra given by

$$E = \frac{\nu}{2\Omega d^2}, \quad Pr = \frac{\nu}{\kappa}, \quad Pm = \frac{\nu}{\eta}, \quad Ra = \frac{\alpha g \beta d^4}{\nu\kappa}, \tag{1}$$

where g is gravity and β is the temperature gradient at the outer boundary.

The parameters that define the dynamo simulations used in this study are summarised in Table 1. Some of these models have been reported before (Davies et al., 2008; Davies and Gubbins, 2011) and some are new. All simulations employ a no-slip outer boundary that is electrically insulating with the heat-flux fixed. On the inner boundary a no-slip condition is imposed in all models, while both conducting and insulating magnetic boundary conditions and temperature and heat-flux thermal boundary conditions are included. Five models employ a spatially non-uniform heat-flux pattern on the outer boundary. The heat-flux pattern is derived from maps of shear-wave anomalies in the lowermost mantle (Masters et al., 1996) and is dominated by spherical harmonic degree and order two. The amplitude of the lateral variations is measured by ϵ, the ratio of peak-to-peak boundary variations and mean outer boundary heat-flux. Further details of the numerical model can be found in Willis et al. (2007) and Davies et al. (2011).

Previous studies have found that the value of the magnetic Reynold's number, Rm, is important for obtaining Earth-like dynamos (Christensen et al., 2010; Olson et al., 2012). Rm is an output of the simulation and is given by

$$Rm = \frac{Ud}{\eta}, \tag{2}$$

where U is a characteristic velocity. Estimating U based on the RMS velocity just below the CMB obtained from core flow inversions gives $U = 3.8 - 5 \times 10^{-4}$ ms^{-1} (Holme, 2007). Together with $\eta = 0.7$ m^{2}s^{-1} (Pozzo et al., 2012, 2013), $Rm \approx 1200 - 1500$. In geodynamo simulations U is usually estimated as the RMS velocity averaged over the whole shell. With this definition Christensen and Tilgner (2004) obtained $Rm \approx 1000$ from a scaling analysis of a suite of geodynamo simulations.

Obtaining numerical dynamos with such high values of Rm is a significant challenge, requiring high Ra and hence high numerical resolution. This inevitably leads to short run times. The highest values of Rm used in this study are $\sim$600 (Table 1), which is a necessary compromise when investigating long-term dynamo behaviour.

Figure 1 illustrates our suite of simulations (details are in Table 1), which follows Christensen et al. (2010) by plotting $E_\eta = E/Pm$ against Rm. Dashed lines delineate the region found by Christensen et al. (2010) to contain Earth-like simulations as defined in Section 3. Most of the model runs exhibit a stable dipolar field and do not reverse, although the suite does include some in the reversing dipole-dominated regime and reversing multipolar regimes identified by Olson and Christensen (2006). The run times in some cases are so short that the simulations cannot be expected to exhibit reversals. In §3 we compare these simulations to the geomagnetic field at appropriate timescales.

3. Comparing Geodynamo Simulations and Geomagnetic Data

To compare simulation outputs with data the synthetic timestep must be rescaled into dimensional units. We are interested in the evolution of the magnetic field so it is natural to consider the two timescales that characterise diffusion and advection of magnetic field, each representing fundamental physical process in Earth's core, and given respectively by

$$\tau^d = \frac{d^2}{\eta}, \qquad \text{and} \qquad \tau^a = \frac{d}{U}, \tag{3}$$

The ratio of these two timescales is the magnetic Reynold's number, $Rm = \tau^d/\tau^a$. In our simulations dimensionless time t^* is measured in units of the magnetic diffusion time, $t^* = t/\tau^d$ where t is dimensional time, which may be converted to advective time units by $t^* = t/(Rm\tau^a)$.

Both advective (Lhuillier et al., 2011, 2013) and diffusive (e.g. Bloxham, 2000; Davies et al., 2008; Driscoll and Olson, 2009; Olson et al., 2013) scaling have been used in the past. Previous works that compared the relative merits of both scalings have advocated the advective scaling when studying relatively short term field variations. Olson et al. (2012) also noted particularly good agreement with advective scaling in the high frequency regime, but found that "there is little to choose between the two scalings at low frequencies". In the following subsections we scale time in our suite of numerical simulations using both the diffusive and advective timescales:

$$t^d = \tau_E^d t^* \qquad \textit{diffusive scaling} \tag{4}$$

$$t^a = \tau_E^d t^* \frac{Rm_m}{Rm_E} \qquad \textit{advective scaling} \tag{5}$$

We take $\tau_E^d = 2 \times 10^5$ yrs (Pozzo et al., 2013) and $Rm_E = 10^3$ (Christensen and Tilgner, 2004).

3.1. Morphological Comparisons with Historical and Millennial Observational Field Models

In this section we compare our suite of numerical simulations with global time-dependent geomagnetic field models using the four quantities proposed by Christensen et al. (2010) (hereafter CAH). The first three are derived from the spatial power spectrum at the CMB,

$$R(l, r_o) = (l+1) \sum_{m=0}^{l} \left(\frac{r_e}{r_o}\right)^{2l+4} [(g_l^m)^2 + (h_l^m)^2], \tag{6}$$

where g_l^m and h_l^m are Gauss coefficients of degree l and order m, r_e is the radius of the Earth , r_o is the CMB radius, and L is maximum harmonic degree. The fourth measures the extent to which magnetic flux on the CMB is concentrated into patches. The four quantities are:

1. AD/NAD: the ratio of power in the axial dipole, AD ($l = 1, m = 0$), to the rest of the field, NAD;
2. O/E: the ratio of the power in equatorially antisymmetric nondipole components, O (coefficients with $l - m$ odd) to the power in equatorially symmetric nondipole components, E ($l - m$ even);
3. Z/NZ: the ratio of power in nondipole zonal, Z ($m = 0$), to nondipole nonzonal, NZ ($m \neq 0$), components;
4. FCF: $(< B_r^4 > - < B_r^2 >^2) \,/ < B_r^2 >^2$, where B_r is the radial component of the magnetic field and angled brackets denote the average over a spherical surface.

The choice of quantities reflect the special significance of the axial dipole field, the equatorial symmetry properties of a magnetic field generated in a spherical shell (Gubbins and Zhang, 1992), and the prominence of intense patches of magnetic flux in historical (Jackson et al., 2000) and archeomagnetic (Korte and Holme, 2010; Amit et al., 2011) field models.

CAH measure the agreement between a simulated field and the geomagnetic field through the normalised squared logarithmic deviation of each simulated quantity P_i from its value derived from an observational field model, P_i^E:

$$\chi^2 = \sum_{i=1}^{4} [(\ln P_i - \ln P_i^E) / \ln \sigma_i]^2, \tag{7}$$

where i represents the criteria (1)–(4) and σ_i is the standard deviation of quantity i. P_i^E and σ_i are calculated from Gauss coefficients of the gufm1 and CALS3k.4b models averaged over 400 and 3000 yrs respectively. The agreement between a simulation and an observational field model is defined as "excellent" if $\chi^2 < 2$, "good" if $\chi^2 < 4$, and "poor" otherwise.

To compute the quantities (1)–(4) Gauss coefficients for the numerical simulations are calculated by upward continuing the radial component of the poloidal field from $r_{\rm o}$ to $r_{\rm e}$. It is well-known that rescaling the dimensionless coefficients is non-unique. We choose to keep the synthetic coefficients in dimensionless form and instead nondimensionalise the observational field models. The scaling factor $\sqrt{2\rho\Omega\mu_0\eta}$ we use is the same as that used to nondimensionalise the simulation equations, where $\rho = 10^4$ kg m^{-3} is the average outer core density and $\Omega = 7.272 \times 10^{-5}$ s^{-1} is the rotation frequency. Note that the quantities (1)–(4) are all relative and do not depend on any choice of scaling for the Gauss coefficients.

We compare simulations to the 400 yr gufm1 model and the 3000 yr CALS3k.4b model using the following strategy. We first rescale time in the dimensionless series for each simulation using both the diffusive scaling (equation (4)) and the advective scaling (equation (5)). We then split the dimensional time-series into bins of length 400 yrs or 3000 yrs and average the Gauss coefficients over each bin. The new time-series of coefficients g_l^m and h_l^m, each averaged over 400 or 3000 yr intervals, are used in (6). For gufm1 the series in (6) is truncated at $L = 8$, as in CAH. For CALS3k.4b the series is truncated at $L = 4$, reflecting the lower resolution of this model (Korte and Constable, 2008). Because the starting time in each simulation is arbitrary we require that each model contain a minimum of one interval with $\chi^2 < 4$ to be judged compatible with the observed field; such intervals, obtained independently when comparing to gufm1 and CALS3k.4b, must also overlap.

Figure 2 shows time-series of χ^2 for three geodynamo simulations using the diffusive scaling (4). Each of the criteria vary significantly with time. The first simulation (model B3 in Table 1) has $E_\eta = 5 \times 10^{-5}$ and $Rm = 475$ and plots inside the wedge-shaped region in Figure 1. The simulation spans 440 kyrs, but we found no time interval with $\chi^2 < 4$ when comparing to gufm1 or CALS3k.4b. This is because magnetic flux is concentrated into many small-scale patches, while the axial dipole is generally much weaker than the observed field. This result is independent of positions for the boundaries of the averaging intervals. The second simulation (model C4 in Table 1) has $E_\eta = 1.2 \times 10^{-5}$ and $Rm = 130$ and plots outside the wedge-shaped region in Figure 1. Nevertheless, agreement between this simulation and gufm1 (CALS3k.4b) was classed as excellent in 11 (8) intervals and good in 92 (36) intervals. The final simulation in Figure 2 (model F2 in Table 1) has $E_\eta = 2 \times 10^{-5}$ and $Rm = 500$, plots inside the wedge-shaped region in Figure 1 and displays low values of χ^2 across the course of the simulation. Excellent agreement with gufm1 and CALS3k.4b is obtained at a number of intervals.

Table 1 shows for each simulation the number of intervals with $\chi^2 < 4$ expressed as a percentage of the total number of intervals. These quantities, denoted $\%(\chi^2)$, are shown for both the diffusion and advective time scalings and for comparisons with gufm1 and CALS3k.4b. For the diffusive scaling only two of the 31 simulations achieve a $\chi^2 < 4$ in more than half the intervals when compared to gufm1; comparing with CALS3k.4b reduces this to one. Values of $\%(\chi^2)$ are systematically lower when the advective time scaling (equation (5)) is used. This is not surprising because all of our models have a lower Rm than the Earth. With the advective time scaling only one model achieves a $\chi^2 < 4$ in more than half the intervals when compared to gufm1; comparing for CALS3k.4b reduces this to zero. In our simulations the generated fields are generally morphologically different from the modern observed field.

We find that a wide range of simulations comply with the CAH criteria in at least one interval for both diffusive and advective timestep scalings. Results for the diffusive scaling are summarised in Figure 1. The majority of simulations with $\chi^2 < 4$ plot inside the wedge-shaped region. Other simulations, such as C4 in Figure 2, plot outside the wedge but still achieve $\chi^2 < 4$. Four of the five simulations with heterogeneous outer boundary heat-flux are in this category; $\chi^2_{AD/NAD}$ and $\chi^2_{O/E}$ vary significantly over time in these models, while χ^2_{FCF} and $\chi^2_{Z/NZ}$ are persistently low because the heterogeneous boundary condition tends to concentrate magnetic flux into pairs of equatorially symmetric patches. We did not find any interval in each of the 5 simulations with $E > 10^{-4}$ that agreed with the CALS3k.4b field. A shorter interval with $\chi^2 < 4$ may exist somewhere in the time-series or might emerge if the simulations were run for longer; however, we choose not to study these models further given the present evidence. For now we regard all 19 simulations with $\chi^2 < 4$ (shown by the grey and open symbols in Figure1) as candidates for further analysis.

3.2. Comparisons based on Frequency Dependence of Variations in the Axial Dipole Moment

We now introduce a new criterion that measures the agreement between temporal variations in the simulations and the geomagnetic field on long timescales. As already noted we compare to the model PADM2M, which describes the temporal evolution of the axial dipole moment over the past 2 Myr (Ziegler et al., 2011); results are also presented for the 800 kyr model Sint-800 (Guyodo and Valet, 1999) and the 2 Myr Sint-2000 model (Valet et al., 2005). We first convert to a time-series of g_1^0 by multiplying the axial dipole moment (ADM) of each model by $\mu_0/(4\pi r_\mathrm{e})$, where μ_0 is the permeability of free space. We then nondimensionalise g_1^0 as described in §3.1 for comparison with the dimensionless g_1^0 output from geodynamo simulations. Our criterion for agreement between simulations and data is based on a comparison of the power spectral density (PSD) of g_1^0.

As in Constable and Johnson (2005) our spectral estimates are computed using the code PSD written by Robert L. Parker (`http://igppweb.ucsd.edu/~parker/Software/index.htm`) which is based on an adaptively smoothed sine multitaper method (Riedel and Sidorenko, 1995) designed to minimize local bias in the spectrum. Several tunable parameters influence the results: 1) whether to prewhiten (pw) the spectra; 2) the spline used for interpolation (Akima or Natural); 3) the smoothness of the PSD, S, which affects the number k of tapers used at each frequency. k also varies with frequency depending on the amount of structure present in the spectrum. Prewhitening is recommended for red spectra (such as the ADM) as it suppresses spectral leakage and this was used to compute the spectra in this paper. We tested how the different choices affect the PSD. The spline choice makes little difference, while the primary impact of the smoothing factor is to improve frequency resolution at the expense of greater uncertainty in spectral amplitude. Prewhitening also changes the low-frequency part of the spectrum, introducing stronger smoothing in that region (and thereby greatly limiting the frequency resolution) and softening the sharpness of the corner transition, while leaving the intermediate- and high-frequency parts relatively unaffected as it should. The basic shape of the spectrum and transition frequencies do not depend strongly on these choices.

Following Olson et al. (2012) we divide the PADM2M spectrum into three frequency ranges: a low frequency (LF) range characterised by a flat spectrum with amplitude a; an intermediate frequency (IF) range where the spectrum follows a power law bf^{-n_b} with $n_b = 2.1 \pm 0.2$, where f is frequency; a high frequency (HF) range where the spectrum follows a power law cf^{-n_c} with $n_c = 6.1 \pm 0.5$ (see Figure 3). Our criterion for agreement is that the PSD of g_1^0 in a geodynamo simulation can be fit by a power law model with exponents that fall within the errors of the PADM2M spectrum, a reasonable measure of the uncertainties.

The corner frequencies are determined by first inspecting the individual spectra to establish frequency ranges that contain the transitions from LF to IF and from IF to HF. In each range the frequency corresponding to the maximum curvature $(\mathrm{d}^2(PSD)/\mathrm{d}f^2)$ is taken as the corner frequency. Error estimates on the fitting parameters for PADM2M are obtained by refitting the data with corner frequencies corresponding to the maximum curvature $\pm \max(\mathrm{d}^2(PSD)/\mathrm{d}f^2)/tol$ where $tol = 2, 5, 10, 100$ is a tolerance. We then obtain power law fits to the PSD between the corner frequencies using least squares (the least squares errors are much smaller than the errors obtained by refitting the spectra). This procedure is repeated for each simulation using first the advective time scaling (5) and then the diffusive scaling (4). Values of a, b, c, n_b, n_c and the corner frequency cf_{li} between LF and IF parts of the spectrum obtained with the diffusive time scaling are given in Table 2 for simulations that meet the criteria in §3.1.

The parameters used to fit the PSD are subject to various sources of uncertainty. Estimates of the low-frequency parameters a and cf_{li} are influenced by tunable parameters in the spectral estimation (see above), the length of the available time-series and differences between ADM models. Table 2 shows that these factors cause estimates of a to vary by over an order of magnitude between Sint-800, Sint-2000 and PADM2M. Moreover, if the available time-series are not long enough to capture the low frequency behaviour of the geodynamo the amplitude a will differ by some unknown amount from the expected value for a longer time-series. The frequency resolution of cf_{li} in PADM2M and Sint-2000 is around 30–40 Myr^{-1}, all other factors being equal; prewhitening increases the uncertainty to $\sim$200 Myr^{-1}. Frequency resolution can be reduced to about $\sim$4 Myr^{-1} by adjusting the smoothing parameter at the expense of greater uncertainty in a and a more complex spectrum. We prefer the relatively smooth prewhitened estimate because of the simplicity of the spectral shape and reduced spectral leakage, despite the poorer frequency resolution. These considerations mean that we do not use the values of a and cf_{li} to define a criterion for temporal agreement between geodynamo simulations and the geomagnetic field (although we note that all dynamo models in Table 2 have values of cf_{li} within the observational errors, while only one model (C5) has a value of a outside the observed range).

Table 2 shows that the HF regions of observational ADM models are not in good agreement, reflecting the different methods by which they were constructed and poor age resolution for paleomagnetic records in the 100 - 1000Myr^{-1} range. However, PADM2M, Sint-800 and Sint-2000 all provide a good sampling of the IF range and we obtain similar fits to the models in this region. We therefore require that our models fit the IF range of the observed ADM models. This amounts to requiring that values of n_b for the geodynamo simulations fall within the range of errors for the observed models. Also, as we are interested in long timescale behaviour, we require that the PSD from simulations contain LF and IF regions.

Figure 3 shows the frequency spectrum of g_1^0 for selected models using respectively the advective and diffusive scalings. These Figures show the result established by Olson et al. (2012) that the advective scaling does the best job of collapsing the spectra in the high-frequency range. [Note that our spectra based on the advective time scaling are shifted towards higher frequencies compared to those based on the diffusive scaling, the opposite to the results in Olson et al. (2012), because we use dimensional time while Olson et al. (2012) use dimensionless time]. At low ($O(10^3 - 10^0)$) frequencies the dispersion of the spectra are comparable for both scalings. The spectra for both scalings show energy at higher frequencies than those in PADM2M. This is expected from the limited temporal resolution achieved by PADM2M. However, the advective spectra are also systematically offset towards higher frequencies with respect to PADM2M but, as is to be expected, the spectral slopes remain unchanged. For the diffusive scaling the spectra plot closer to PADM2M; in particular, the spectra for models with $Rm = 130$ and $Rm = 261$ lie very close to the PADM2M spectrum. Power-law fits, shown by black solid lines, demonstrate that the models in Figure 3 conform to the basic shape of the PADM2M spectrum. This analysis also indicates that the diffusive time scaling is an appropriate choice for making comparisons involving temporal variations at timescales of 10kyr or longer.

Table 2 shows that ADM spectra from 12 of the 19 remaining simulations provide a satisfactory fit to the PADM2M spectrum. Models C1-5, D1, F1 and G1 are too short to fit the LF part of the PADM2M spectrum. In the following sections we focus on the four geodynamo simulations in Figure 3; results for all simulations are listed in Table 2. To simplify the presentation we now focus on results obtained with the diffusive time scaling. We note that this choice does not affect our conclusions regarding the long-term behaviour of our geodynamo models.

4. Long-term variations in geodynamo simulations

We are now in a position to investigate the existence of a time-averaged field (a field that does not change upon further averaging) and to attempt to determine the length of time required to obtain a stable average. We do this for both PADM2M and the simulated fields, first defining the running average of the sum of Gauss coefficients, $\overline{g(t)}$, as

$$\overline{g(t)} = \overline{g(t-1)}\frac{(t-1)}{t} + \frac{1}{t}\sum_{l,m}^{L,M}\left[g_l^m(t) + h_l^m(t)\right], \qquad t = 1, 2, \ldots, n \tag{8}$$

where M is the maximum harmonic order. We define $\overline{g_1^0(t)}$ by setting $L = 1, M = 0$ in (8), while $\overline{g_z(t)}$ and $\overline{g_{nz}(t)}$ are defined by retaining respectively the zonal or nonzonal coefficients in (8) as described in §3.1. To define a time-average, the graph of $\overline{g(t)}$ should tend to a horizontal line as t increases. Small fluctuations will always arise as the length of the time-series is extended. To estimate the time needed to obtain the mean dipole field we define the parameter τ_{ave} as the time after which fluctuations in $\overline{g_1^0(t)}$ do not exceed 1% of the final value of $\overline{g_1^0}$. This strategy will yield an underestimate for short runs.

Figure 4 shows the time variation of g_1^0 and $\overline{g_1^0}$ for PADM2M. Field reversals cause a sudden change in $\overline{g_1^0}$, leading to a lack of stability from $2.0 - 0.78$ Ma when the field reverses regularly. Since the most recent reversal $\overline{g_1^0}$ appears to flatten out; fluctuations reduce to $< 1\%$ of the final value after $\tau_{ave} = 1.8$ Myr of averaging. If the running average is started following the most recent reversal, $\tau_{ave} = 600$ kyr of averaging is required to obtain the mean value of g_1^0. However, as noted by Ziegler et al. (2011) there are differences in the 0.78 Myr and 2 Myr averages, indicating that the power spectrum for the actual field is not flat at long periods.

Figure 5 shows the time variation of $\overline{g_1^0}$ for four geodynamo simulations. The starting time has been picked arbitrarily, but further calculations verify that it does not change the results. In most cases the value of τ_{ave} (see Table 2) is comparable to the length of the simulation (compare to Table 1 with one time unit equal to 2×10^5 yrs for the diffusive scaling). The long-term variations in the running averages shown in Figure 5 suggest that larger values of τ_{ave} may be obtained if the simulations were run for longer. Indeed, it is expected based on the running average for PADM2M that future reversals in models C8 and C10 (which are in the dipole reversing regime) will destabilise the running average, while the values of τ_{ave} obtained for the non-reversing models C1-4 and C4 are already longer than any period of stable polarity covered by PADM2M. Making the assumption that the values of τ_{ave} in Table 2 are robust gives $0.3 \leq \tau_{ave} \leq 2.2$ Myr, which exceeds the magnetic diffusion timescale and amounts to many dipole decay times (magnetic diffusion time divided by π^2 (Olson et al., 2012)).

Figure 5 also shows that the nonzonal component, $\overline{g_{\mathrm{nz}}}$, reduces to less than 2% of $|\overline{g}|$ within ∼400 kyr of averaging in all simulations except the model with $Rm = 564$. The magnitude and variation of $\overline{g_{\mathrm{nz}}}$ is much less than $\overline{g_{\mathrm{z}}}$. After an initial transient period at the start of the running average (not associated with the start of the dynamo simulation) the variations in $\overline{g}$ tend to be reflected in $\overline{g_{\mathrm{z}}}$. By far the biggest contribution to $\overline{g_{\mathrm{z}}}$ is from g_1^0.

We now consider the spatial CMB power spectrum, obtained by averaging the entire time-series of Gauss coefficients for each simulation (Figure 6). Power in equatorially antisymmetric modes, R_{EA}, is much greater than power in equatorially symmetric modes, R_{ES}, in all simulations. R_{EA} is characterised by a zigzag pattern with peaks at odd l . This pattern has been found in other dynamo simulations (Dormy et al., 2000; Christensen and Olson, 2003; Coe and Glatzmaier, 2006; Christensen and Wicht, 2007; Driscoll and Olson, 2009). The zonal spectrum, R_z, has a very similar shape to R_{EA} and further investigation shows that the zonal modes make the dominant contribution to R_{EA}, as could be anticipated from Figure 5. Energy in R_{ES} and R_{nz} increases with Rm, except for the simulation with $Rm = 130$, which includes lateral variations in outer boundary heat-flux. Nevertheless, because power in R_{EA} is greater than power in R_{ES}, the overall spectrum is dominated by EA modes and retains the zigzag pattern. All of our models with a homogeneous outer boundary heat-flux and a zigzag time-averaged spatial spectrum generate time-averaged fields that are axial-dipole dominated with very little non-axisymmetric structure.

A simple measure of the zigzag spectrum is obtained by dividing the sum of odd

l components of the time-averaged nondipole ($l > 1$) power spectrum by the sum of even l components up to degree $L = 10$. This quantity, EA/ES is provided in Table 2 for all models and is generally $\gg 1$, as expected for a spectrum characterised by a zigzag shape. Exceptions to this are model F1, which has been run for less than one time unit, and models C4 and C5, which both incorporate a laterally-varying outer boundary heat-flux. The significance of the outer boundary condition is discussed further below.

The running averages in Figure 5 suggest that the zigzag spectrum may emerge for averaging times much shorter than those required to obtain stable mean fields because the nonzonal and equatorially symmetric contributions average out relatively quickly. Figure 7 shows power spectra averaged over successively longer time periods for four geodynamo simulations. Average spectra are very different from instantaneous spectra because nonzonal and equatorially symmetric terms average out. Surface spectra for model C1-4 ($Rm = 261$) show that the zigzag pattern emerges after 15 kyr and remains thereafter. In this model $l = 7$ is anomalous in the sense that it is low compared to the adjacent even values of $l = 6$ and $l = 8$ modes, while all other odd l up to $l = 10$ are higher than the adjacent even l. The surface spectrum for model C1-4 averaged over 1000 kyr looks very similar to that averaged over 15 kyrs. Models C8 ($Rm = 356$) and C10 ($Rm = 500$) display spectra with the zigzag pattern after 10 and 15 kyr respectively. Model C4 ($Rm = 130$), which includes lateral variations in outer boundary heat-flux, displays the zigzag spectrum in the 3 kyr average but not in the 10, 15 and 20 kyr averages. In this case the h_2^1 and g_3^2 Gauss coefficients are much larger than in the homogeneous geodynamo simulations and make significant contributions to the average spectra (Davies et al., 2008).

5. Discussion and Conclusions

We have used a suite of geodynamo simulations to investigate long-term geomagnetic field behaviour. Simulations were selected based on agreement between the synthetic and observed magnetic fields in terms of five quantities. Four of these were defined by Christensen et al. (2010) and relate to the field morphology. We employed a fifth quantity describing temporal field variations by a power law fit to the frequency spectrum of the axial dipole moment and required that synthetic spectra follow the same power law to within the observationally-determined errors. Seven of 19 models were rejected based on this criterion, indicating a sensitivity that is not overly restrictive.

Our application of the morphological criteria differs from that of Christensen et al. (2010): instead of dealing with the average we treated gufm1 and CALS3k.4b separately and divided all simulation time-series into intervals 400 and 3000 years long, applying the criteria to each interval separately. The misfit ratings vary significantly over time in our simulations. Short term averages can meet the morphological criteria for being Earth-like, leading to conclusions that might not be supported by longer term averages. We also found that some simulations display markedly different levels of agreement for gufm1 and CALS3k.4b. This suggests that each global field model should be treated separately when compared to geodynamo simulations. Similar issues may pertain to comparisons of the dipole moment. We chose to conduct a detailed analysis based on the PADM2M axial dipole moment model (Ziegler et al., 2011); this lengthy process could be attempted for other such models.

Over half of the models rejected on the basis of morphological comparisons, together with the additional criterion for temporal agreement based on the power spectra, lie inside the wedge-shaped region (Figure 1) defined in terms of magnetic Ekman number and magnetic Reynold's number that Christensen et al. (2010) found to contain Earth-like dynamo models (models satisfying the criteria) for their extensive suite of simulations. The region where Earth-like dynamo models exist in $E_\eta - Rm$ space must be bounded from below because there is a minimum Rm for dynamo action; it is likely bounded from above because multipolar fields are generally obtained when the dynamo is strongly driven. Whether there exists a single region of parameter space where simulations exhibit similar spatio-temporal characteristics to the Earth seems to require more work.

It is interesting to note that three of the four simulations with an imposed heterogeneous outer boundary heat-flux and relatively low Rm ($125 - 137$) achieve good morphological similarity ($\chi^2 < 4$ at some time) with the observed field. Of these three models, two also pass our temporal criterion. These models do not reverse, but can produce long-term fluctuations associated with the partial locking of convective structures to the boundary anomalies (Davies et al., 2008). It would be highly desirable to explore heterogeneous boundary conditions at higher Rm to establish whether the excellent morphological agreement persists.

The majority (16/19) of our simulations that successfully match the morphology of the modern field in at least one interval exhibit poor morphological agreement with the observed field over more than half their duration. Extrapolating these results to the geomagnetic field comes with the usual caveats that the simulations operate with parameters that are very different to those pertaining to Earth's core. By selecting simulations based on the five criteria described above we have confidence that the spatio-temporal characteristics of the models resemble those of the data, even if the physics in the model is not completely faithful to the core. Assuming the simulation results can be extrapolated to the Earth, the past field may often have been morphologically different from the modern field.

Simulations satisfying the five criteria were used to investigate the field behaviour on timescales where the nondipole part of the field is poorly constrained by observations. We found that the length of time needed to obtain a converged estimate of the dipole field strength was comparable to the length of the simulation in the majority of cases, including models that did not reverse polarity. Reversals tend to destabilise the running average. These results suggest that long periods of stable polarity spanning many magnetic diffusion times are needed to obtain robust estimates of the mean dipole field strength.

We find that long-term fluctuations in the simulated magnetic fields are due almost entirely to the axial dipole, with the running average of the non-axial dipole field stabilising after only a few tens of kyrs. Furthermore, we find that, in all simulations, the spatial power spectrum at the CMB is characterised by a zigzag pattern with high power in odd harmonic degrees. Our results suggest that this spectral pattern may emerge after as little as $15 - 20$ kyr of averaging. The numbers depend on the choice of scaling for the dimensionless numerical timestep. An alternative scaling based on the advection timescale will give smaller averaging times than the diffusive scaling if Rm in the simulation is smaller than Rm in the Earth (as is the case here), equal if the two values of Rm are equal, and larger otherwise.

Changes in the shape of the CMB power spectrum with increasing averaging time may yield important insights into the long-term morphology of the geomagnetic field. Figure 8 shows surface power spectra for the observational model CALS10k.1b, the longest global model currently available, averaged over several different time intervals. Zigzag patterns in the spectra with dominance by odd degrees can be seen in 1 kyr and 5 kyr averages over some windows but not others; the same is true of the dynamo simulations for these window sizes. However, the 10 kyr-averaged spectrum for CALS10k.1b does not display such a pattern. There are hints that this is due to decreasing model resolution as the model extends further back in time where the inherent lack of resolution with limited data quality and poor coverage in the southern hemisphere is especially pronounced. Alternatively, it may reflect an interesting property about the structure of the geomagnetic field . An observational geomagnetic field model spanning a period of $15-20$ kyr with resolution up to harmonic order 5 would be the ideal test of the predictions made in this work.

Acknowledgements

CD acknowledges a postdoctoral scholarship from the Green Foundation at IGPP and a Natural Environment Research Council personal fellowship, reference NE/H01571X/1. This work was also supported by NSF grants EAR0724331 and EAR1065597. The authors thank Julien Aubert for insightful comments on an earlier version of the manuscript and Alex Fournier and an anonymous reviewer for detailed and constructive reviews. CD thanks Luis Silva and Peter Driscoll for stimulating discussions.

References

Alexandrescu, M., Gibert, D., Hulot, G., Le Mouel, Saracco, G., 1995. Detection of geomagnetic jerks using wavelet analysis. J. Geophys. Res. 100, 12557–12572.

Amit, H., Korte, M., Aubert, J., Constable, C., Hulot, G., 2011. The time-dependence of intense archeomagnetic flux patches. J. Geophys. Res. 116, B12106.

Biggin, A., Steinberger, B., Aubert, J., Suttie, N., Holme, R., Torsvik, T., van der Meer, D., van Hinsbergen, D., 2012. Possible links between long-term geomagnetic variations and whole-mantle convection processes. Nat. Geosci. 5, 526–533.

Bloxham, J., 2000. The effect of thermal core-mantle interactions on the palaeomagnetic secular variation. Phil. Trans. R. Soc. Lond. A 358, 1171–1179.

Bloxham, J., Jackson, A., 1992. Time-dependent mapping of the magnetic field at the core-mantle boundary. J. Geophys. Res. 97, 19537–19563.

Cande, S., Kent, D., 1992. A new geomagnetic polarity time scale for the late cretaceous and cenozoic. J. Geophys. Res. 97, 13917–13951.

Cande, S., Kent, D., 1995. Revised calibration of the geomagnetic polarity timescale for the late cretaceous and cenozoic. J. Geophys. Res. 100, 2156–2202.

Christensen, U., Aubert, J., Hulot, G., 2010. Conditions for Earth-like geodynamo models. Earth Planet. Sci. Lett. 296, 487–496.

Christensen, U., Olson, P., 2003. Secular variation in numerical geodynamo models with lateral variations of boundary heat flow. Phys. Earth Planet. Int. 138, 39–54.

Christensen, U., Tilgner, A., 2004. Power requirement of the geodynamo from ohmic losses in numerical and laboratory dynamos. Nature 439, 169–171.

Christensen, U., Wicht, J., 2007. Numerical dynamo simulations. In: Schubert, G. (Ed.), Treatise on Geophysics Vol. 8. Elsevier, Amsterdam, pp. 245–282.

Coe, R., Glatzmaier, G., 2006. Symmetry and stability of the geomagnetic field. Geophys. Res. Lett. 33, L21311.

Constable, C., 2011. Modelling the geomagnetic field from syntheses of paleomagnetic data. Phys. Earth Planet. Int. 187, 109–117.

Constable, C., Johnson, C., 2005. A paleomagnetic power spectrum. Phys. Earth Planet. Int. 153, 61–73.

Davies, C., Gubbins, D., 2011. A buoyancy profile for the Earth's core. Geophys. J. Int. 187, 549–563.

Davies, C., Gubbins, D., Jimack, P., 2011. Scalability of pseudospectral methods for geodynamo simulations. Concurrency Computat.: Pract. Exper. 23, 38–56.

Davies, C., Gubbins, D., Willis, A., Jimack, P., 2008. Time-averaged paleomagnetic field and secular variation: Predictions from dynamo solutions based on lower mantle seismic tomography. Phys. Earth Planet. Int. 169, 194–203.

Dormy, E., Valet, J., Courtillot, V., 2000. Numerical models of the geodynamo and observational constraints. Geochemistry, Geophysics, Geosystems 1, 1–42.

Driscoll, P., Olson, P., 2009. Polarity reversals in geodynamo models with core evolution. Earth Planet. Sci. Lett. 282, 24–33.

Gallet, Y., Hulot, G., Chulliat, A., Genevey, A., 2009. Geomagnetic field hemispheric asymmetry and archeomagnetic jerks. Earth Planet. Sci. Lett. 284, 179–186.

Glatzmaier, G., 2002. Geodynamo simulations–How realistic are they? Annu. Rev. Earth Planet. Sci. 30, 237–257.

Glatzmaier, G., Coe, R., 2007. Magnetic polarity reversals in the core. In: Schubert, G. (Ed.), Treatise on Geophysics. Elsevier, pp. 283–297.

Gubbins, D., Willis, A., Sreenivasan, B., 2007. Correlation of Earth's magnetic field with lower mantle thermal and seismic structure. Phys. Earth Planet. Int. 162, 256–260.

Gubbins, D., Zhang, K., 1992. Symmetry properties of the dynamo equations for palaeomagnetism and geomagnetism. Phys. Earth Planet. Int. 75, 225–241.

Guyodo, Y., Valet, J.-P., 1999. Global changes in intensity of the Earth's magnetic field during the past 800 kyr. Nature 399, 249–252.

Holme, R., 2007. Large-scale flow in the core. In: Schubert, G. (Ed.), Treatise on Geophysics Vol. 8. Elsevier, pp. 107–130.

Jackson, A., Jonkers, A., Walker, M., 2000. Four centuries of geomagnetic secular variation from historical records. Phil. Trans. R. Soc. Lond. A 358, 957–990.

Kono, M., Roberts, P., 2002. Recent geodynamo simulations and observations of the geomagnetic field. Rev. Geophys. 40, 1013–1061.

Korte, M., Constable, C., 2003. Continuous global geomagnetic field models for the past 3000 years. Phys. Earth Planet. Int. 140, 73–89.

Korte, M., Constable, C., 2005. Continuous geomagnetic field models for the past 7 millennia: 2. CALS7K. Geochem. Geophys. Geosys 6, 1–18.

Korte, M., Constable, C., 2006. Centennial to millennial geomagnetic secular variation. GJI 167, 43–52.

Korte, M., Constable, C., 2008. Spatial and temporal resolution of millennial scale geomagnetic field models. Advances in Space Research 41, 57–69.

Korte, M., Constable, C., 2011. Improving geomagnetic field reconstructions for 0-3 ka,. Phys. Earth Planet. Int. 188, 247–259.

Korte, M., Constable, C., Donadini, F., Holme, R., 2011. Reconstructing the holocene geomagnetic field. Earth Planet. Sci. Lett. 312, 497–505.

Korte, M., Holme, R., 2010. On the persistence of geomagnetic flux lobes in global holocene field models. Phys. Earth Planet. Int. 182, 179–186.

Kutzner, C., Christensen, U., 2002. From stable dipolar towards reversing numerical dynamos. Phys. Earth Planet. Int. 131, 29–45.

Laj, C., Kissel, C., Davies, C., Gubbins, D., 2011. Geomagnetic field intensity and inclination records from Hawaii and the Réunion island: Geomagnetic implications. Phys. Earth Planet. Int. 187, 170–187.

Lhuillier, F., Fournier, A., Hulot, G., Aubert, J., 2011. The geomagnetic secular-variation timescale in observations and numerical dynamo models. Geophys. Res. Lett. 38.

Lhuillier, F., Hulot, G., Gallet, Y., 2013. Statistical properties of reversals and chrons in numerical dynamos and implications for the geodynamo. Phys. Earth Planet. Int. 220, 19–36.

Malin, S., Hodder, B., 1982. Was the 1970 geomagnetic jerk of internal or external origin? Nature 296, 726–728.

Masters, G., Johnson, S., Laske, G., Bolton, H., 1996. A shear-velocity model of the mantle. Phil. Trans. R. Soc. Lond. A 354, 1385–1411.

McMillan, D., Constable, C., Parker, R., Glatzmaier, G., 2001. A statistical analysis of magnetic fields from some geodynamo simulations. Geochem. Geophys. Geosys. 2.

Olsen, N., Mandea, M., Sabaka, T., Tøffner-Clausen, T., 2010. The CHAOS-3 geomagnetic field model and candidates for IGRF-2010. Earth Planets Space 62 (IGRF Special issue), 719–727.

Olson, P., Christensen, U., 2002. The time-averaged magnetic field in numerical dynamos with non-uniform boundary heat flow. Geophys. J. Int. 151, 809–823.

Olson, P., Christensen, U., 2006. Dipole moment scaling for convection-driven planetary dynamos. Earth Planet. Sci. Lett. 250, 561–571.

Olson, P., Christensen, U., Driscoll, P., 2012. From superchrons to secular variation: A broadband dynamo frequency spectrum for the geomagnetic dipole. Earth Planet. Sci. Lett. 319–320, 75–82.

Olson, P., Deguen, R., Hinnov, L., Zhong, S., 2013. Controls on geomagnetic reversals and core evolution by mantle convection in the Phanerozoic. Phys. Earth Planet. Int. 2‘14, 87–103.

Pozzo, M., Davies, C., Gubbins, D., Alfè, D., 2012. Thermal and electrical conductivity of iron at Earth's core conditions. Nature 485, 355–358.

Pozzo, M., Davies, C., Gubbins, D., Alfè, D., 2013. Transport properties for liquid silicon-oxygen-iron mixtures at Earth's core conditions. Phys. Rev. B 87, 014110.

Riedel, K., Sidorenko, A., 1995. Minimum bias multiple taper spectral estimation. IEEE Trans Sig. Proc., 43, 188–195.

Valet, J., Meynadier, L., Guyodo, Y., 2005. Geomagnetic dipole strength and reversal rate over the past two million years. Nature 435, 802–805.

Willis, A., Sreenivasan, B., Gubbins, D., 2007. Thermal core-mantle interaction: exploring regimes for 'locked' dynamo action. Phys. Earth Planet. Int. 165, 83–92.

Ziegler, L., Constable, C., 2011. Asymmetry in growth and decay of the geomagnetic dipole. Earth Planet. Sci. Lett. 213, 300–304.

Ziegler, L., Constable, C., Johnson, C., Tauxe, L., 2011. PADM2M: a penalized maximum likelihood model of the 0-2 Ma palaeomagnetic axial dipole moment. Geophys. J. Int. 184, 1069–1089.

Label	E	Pm	Pr	RaE	H	ϵ	BC	Rm	T	Reg	$\%(\chi^2)^d_g$	$\%(\chi^2)^d_c$	$\%(\chi^2)^a_g$	$\%(\chi^2)^a_c$
A1	1	1	0.1	40	B	0	TF	78	100	DN	0.04	0.0	0.0	0.0
B1	0.5	1	0.1	150	B	0	TF	278	9	DR	1.3	0.0	2.5	0.0
B2	0.5	10	1	200	B	0	TF	326	2	DN	0.3	0.0	0.5	0.0
B3	0.5	10	1	400	B	0	TF	475	1.2	DR	0.0	0.0	0.0	0.0
B4	0.5	5	1	300	B	0	TF	227	8	MR	0.0	0.0	0.0	0.0
C1-2*	0.12	2	1	20	B/I	0	TF	126	8	DN	73.9	39.2	57.4	14.9
C1-3*	0.12	2	1	50	B/I	0	TF	199	8	DN	58.7	0.1	39.4	0.0
C1-4*	0.12	2	1	100	B/I	0	TF	261	4.2	DN	36.8	13.5	22.0	2.3
C1-5*	0.12	2	1	200	B/I	0	TF	650	0.3	DR	7.5	10.3	9.1	5.0
C2-2*	0.12	2	1	20	B/I	0	TF	78	10	DN	0.1	43.3	0.0	6.3
C2-3*	0.12	2	1	50	B/I	0	TF	105	3	DN	39.5	52.9	6.2	16.7
C2-5*	0.12	2	1	200	B/I	0	TF	269	0.6	DN	41.4	19.7	30.0	5.0
C3-2*	0.12	2	1	20	B	0	TF	72	12	DN	28.5	39.9	4.7	15.2
C3-3*	0.12	2	1	50	B	0	TF	102	10	DN	25.0	7.9	14.1	5.9
C3-4*	0.12	2	1	100	B	0	TF	153	2	DN	46.0	14.6	34.7	7.7
C3-5*	0.12	2	1	200	B/I	0	TF	427	1	MR	0.0	0.0	0.0	0.0
C4	0.12	10	1	34.9	I	0.3	TF	130	10	DN	2.1	4.9	0.9	0.0
C5	0.12	10	1	34.9	I	0.6	TF	125	6.5	DN	3.1	5.9	1.9	2.9
C6	0.12	10	1	57.5	I	0.6	TF	192	1.4	DN	0.3	0.0	0.0	0.0
C7	0.12	10	1	34.9	I	0.9	TF	137	10	DN	5.3	3.0	3.5	0.0
C8	0.12	10	1	150	B	0	TF	356	2	DR	4.5	3.4	5.2	2.9
C9	0.12	10	1	150	B	0.9	TF	353	2	DN	0.0	0.0	0.0	0.0
C10	0.12	10	1	300	B	0	TF	564	1.8	DR	11.6	15.2	12.8	14.8
D1	0.10	3	1	350	B	0	FF	154	0.5	-	2.1	1.1	0.8	0.0
D2	0.10	3	1	255	B	0	TF	192	0.1	-	5.9	0.0	3.0	0.0
E1	0.06	3	1	765	B	0	FF	264	0.1	-	14.3	0.0	8.4	0.0
E2	0.06	3	1	380	B	0	FF	164	0.2	-	7.8	0.0	3.9	0.0
E3	0.06	2	1	765	B	0	FF	184	0.2	-	15.4	0.0	8.5	0.0
F1	0.02	1	0.1	60	I	0	TF	198	1	DN	47.0	29.1	40.0	16.7

F2	0.02	1	0.1	240	B	0	TF	500	0.5	-	27.3	21.1	27.9	18.2
G1	0.005	1	0.1	120	B	0	TF	401	0.1	-	22.0	7.1	8.3	16.7

Table 1: Geodynamo simulations used in this work. E = Ekman number ($\times 10^{-3}$); Pm = magnetic Prandtl number; Pr = Prandtl number; Ra = Rayleigh number. H= heating mode used to drive the dynamo: bottom heating (B) or internal heating (I). ϵ = amplitude of thermal anomalies imposed at the outer boundary; $\epsilon = 0$ refers to a homogeneous outer boundary, otherwise the pattern is derived from seismic tomography. BC= thermal boundary condition with the first letter referring to the inner boundary and the second letter referring to the outer boundary: T=fixed temperature; F=fixed heat-flux. $Rm = \sqrt{(2E_K/V_s)}$, the magnetic Reynolds number, where E_K is the time-averaged nondimensional kinetic energy and $V_s = 14.59$ is the nondimensional volume of the fluid shell. T= length of the simulation in units of d^2/η. Reg= dynamo regime following Olson and Christensen (2006): DN=dipole-dominated, non-reversing; DR=dipole-dominated, reversing; MR=multipolar, reversing. $\%(\chi^2)$ indicates the percentage of windows with $\chi^2 < 4$ when comparing to gufm1 (subscript g) and CALS3k.4b (subscript c) using the diffuse time scaling (superscript d) and advective time scaling (superscript a). Simulations denoted by an asterisk are driven by buoyancy profiles described in Davies and Gubbins (2011) where the formulation for the basic heating model can be found. Further description of the simulations can be found in the text.

Label	Rm	a	b	n_b	c	n_c	cf_{li}	τ_{ave}	EA/ES
C1-2	126	0.4	0.03	-2.0	80	-6.4	9	0.6 (0.08)	148
C1-3	199	0.3	0.009	-1.6	80	-6.0	9	0.8 (0.2)	193
C1-4	261	1.4	0.07	-2.2	80	-5.8	6	0.9 (0.3)	156
C1-5	650	-	1.72	-2.3	60	-5.5	-	-	-
C2-2	78	1.2	0.04	-2.2	52	-4.6	2	1.2 (0.1)	125
C2-3	105	1.2	0.03	-2.3	80	-6.7	4	0.5 (0.06)	21
C2-5	269	0.2	0.006	-1.6	80	-5.9	9	0.3 (0.1)	14
C3-2	72	0.5	0.03	-2.0	80	-6.5	2	2.2 (0.2)	71
C3-3	102	0.5	0.07	-2.1	80	-6.5	11	0.3 (0.03)	65
C3-4	153	0.3	0.11	-2.0	80	-6.2	19	0.4 (0.07)	38
C4	130	2.8	0.19	-2.1	80	-6.3	8	1.9 (0.2)	6
C5	125	130	0.06	-1.9	9	-6.0	2	2.2 (0.3)	2
C7	137	1.0	0.01	-1.8	80	-6.4	3	0.7 (0.1)	7
C8	356	0.9	3.51	-2.2	80	-6.5	27	0.3 (0.1)	114
C10	564	0.1	1.00	-1.9	950	-6.5	38	0.3 (0.2)	77
D1	154	-	0.94	-3.8	3	-7.0	-	-	-
F1	198	-	3.10	-2.2	80	-5.4	-	-	-
F2	500	0.7	3.44	-2.2	200	-5.6	52	0.07 (0.04)	7
G1	401	-	0.20	-2.9	70	-4.9	-	-	-
Sint-800		0.39	0.07	-1.9	500	-6.0	14.1		
Sint-2000		1.35	0.27	-2.3	4.2×10^{-9}	-3.0	9.8		
Sint-2000^{+}		1.63	0.07	-1.9	2.3×10^{-10}	-2.1	8.3		
PADM2M		0.99	0.08	-2.1	3	-6.2	7.7	0.6 (Brunhes)	
				± 0.2		± 0.5	± 210	1.8 (2 Myr)	
PADM2M^{+}		0.58	0.07	-2.1	4	-6.3	10.1	0.6 (Brunhes)	
				± 0.2		± 0.5	± 53	1.8 (2 Myr)	

Table 2: Fitting parameters a ($\times 10^{-6}$), b ($\times 10^{-3}$), c ($\times 10^{5}$), n_b and n_c that give the best-fitting power-law spectrum to PADM2M for each simulation. cf_{li} (Myr^{-1}) denotes the corner frequency between low-frequency and intermediate-frequency parts of the power spectrum. τ_{ave} (Myr) denotes the time after which fluctuations in $\overline{g_1^0}$ did not exceed 1% of the final value of $\overline{g_1^0}$. τ_{ave} is given for the both diffusive and advective (in brackets) scalings of the model time. EA/ES denotes the ratio of total power in equatorially antisymmetric to equatorially symmetric components of the time-averaged nondipole power spectrum up to degree $L = 10$. Dashes indicate that the quantity was not calculated because the model did not fit the power law model for PADM2M based on the criterion described in §3.2, while models highlighted in green are deemed successful based on this criterion. $^{+}$ indicates that the spectrum was not prewhitened.

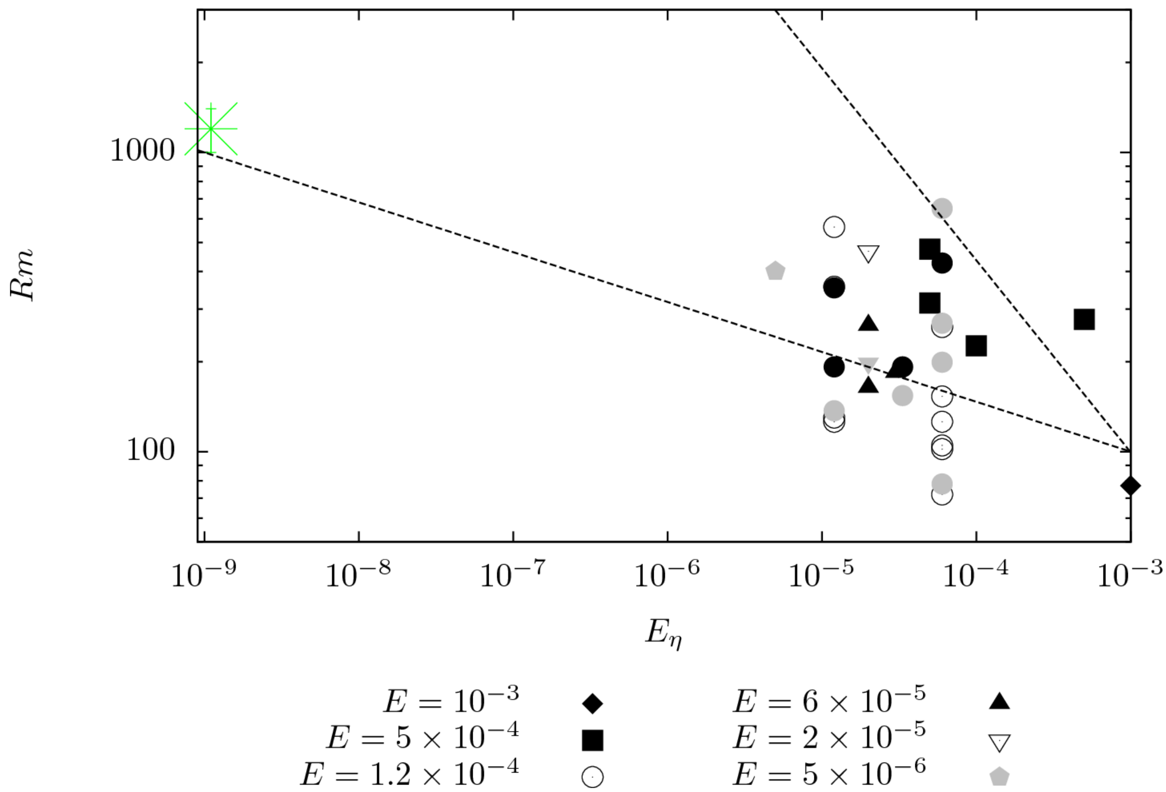

Figure 1: Dynamo models used in this study plotted as a function of magnetic Ekman number E_η and magnetic Reynold's number Rm following Christensen et al. (2010). Open symbols denote models where the morphological agreement between a simulated field and the fields of both gufm1 and CALS3k.4b was either good or excellent ($\chi^2 < 4$) and where the synthetic dipole moment power spectrum provided a satisfactory fit to the spectrum of PADM2M. Models with black symbols were found to give poor morphological compliance, while models with grey symbols gave either good or excellent morphological compliance but did not provide a satisfactory fit to the PADM2M dipole moment spectrum. The dashed lines delineate the wedge-shaped region found by Christensen et al. (2010) to contain simulations with $\chi^2 < 4$. The large asterisk denotes the values of Rm and E_η estimated for the Earth.

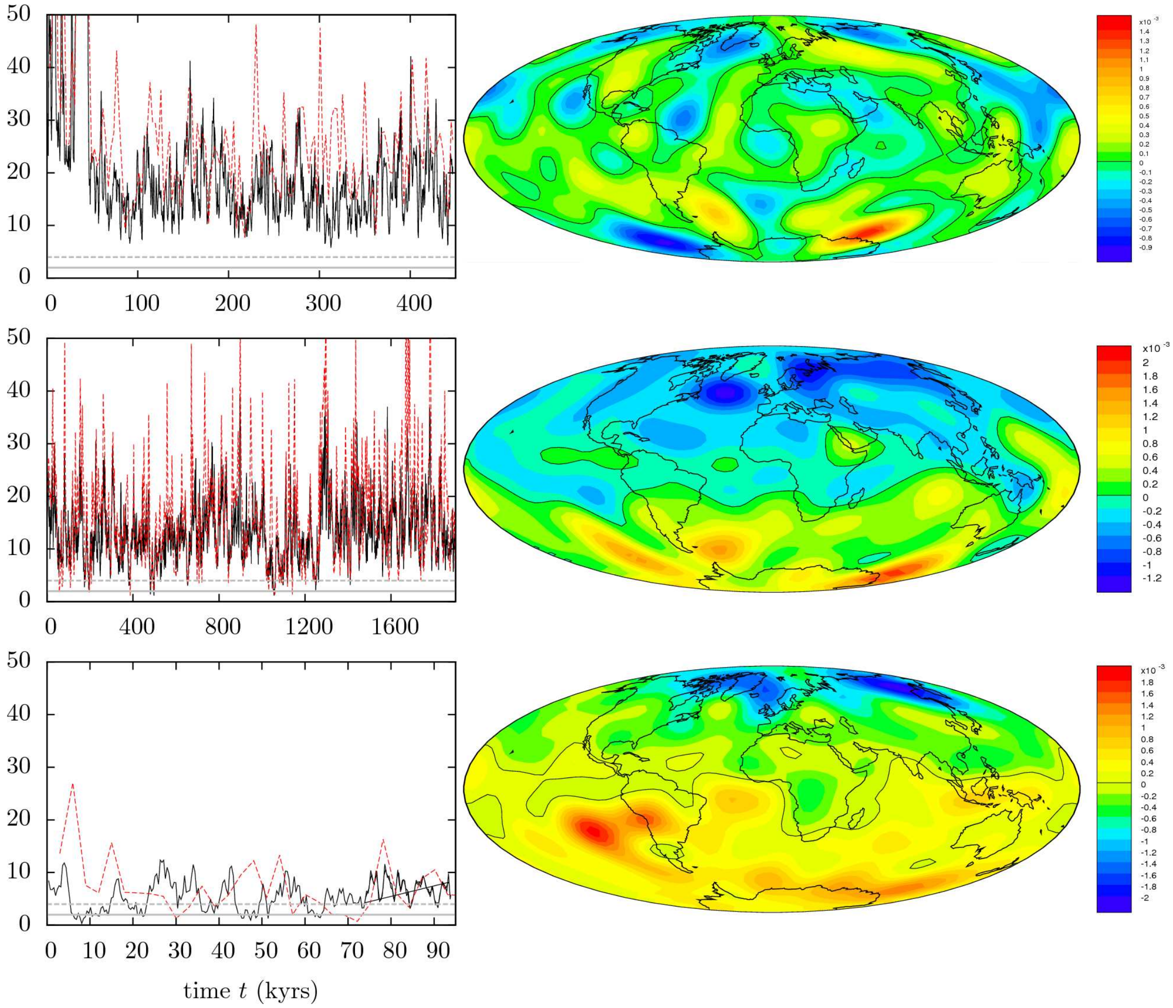

Figure 2: χ^2 rating (left column) for three numerical geodynamo simulations. Black lines show the final rating for each model when compared to gufm1; red dashed lines for CALS3k.4b; horizontal lines indicating excellent ($\chi^2 = 2$) and good ($\chi^2 = 4$) agreement. The right column shows the radial magnetic field B_r at the outer boundary for a single interval of 400 yrs plotted to spherical harmonic degree $L = 12$. The three dynamo simulations are: model B3 (top), C4 (middle) and F2 (bottom). The diffusion time scaling τ^d has been used to scale the time axis. Further details of the models can be found in Table 1.

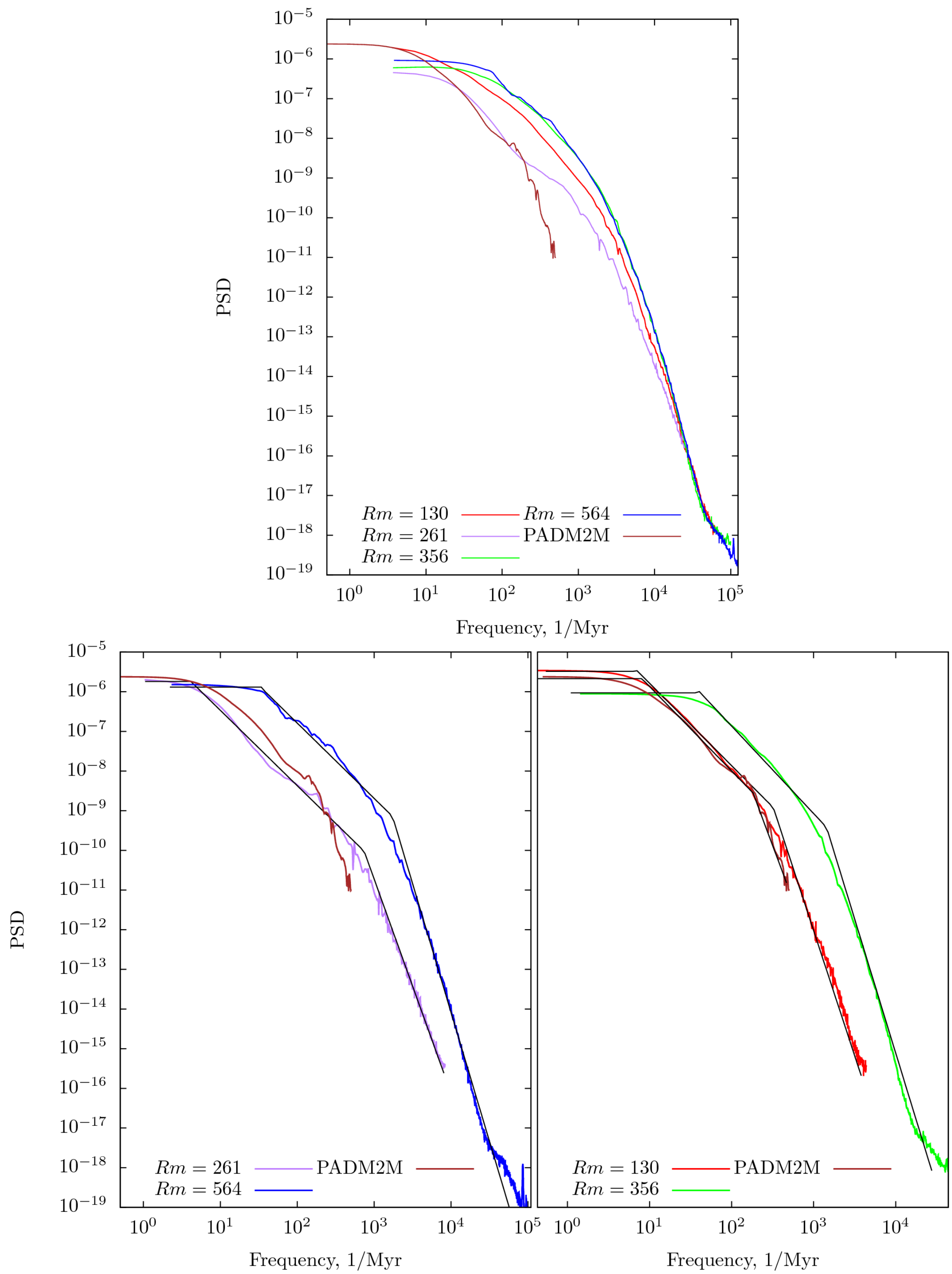

Figure 3: Dimensionless power spectral density (PSD) of the axial dipole magnetic field plotted against frequency f in Myr^{-1} for the geodynamo simulations C4 ($Rm = 130$), C1-4 ($Rm = 261$), C8 ($Rm = 356$) and C10 ($Rm = 564$) in Table 1, which satisfy the criteria of Christensen et al. (2010). In the top panel the simulation time has been scaled by the advection timescale, τ^a. In the bottom panels simulation time has been scaled by the diffusive timescale, τ^d, and solid black lines show best-fit power-law models based on the spectrum of PADM2M. See text for further details.

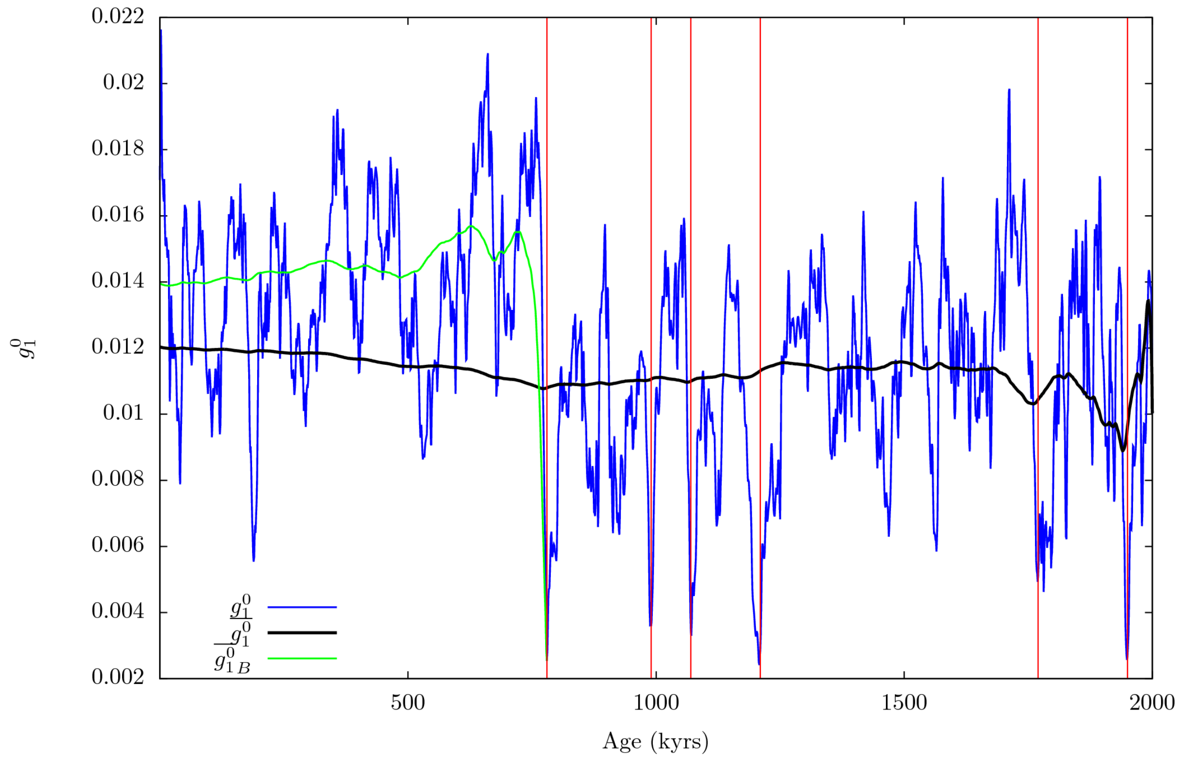

Figure 4: Time-series of g_1^0 (blue line) and the running average of g_1^0, $\overline{g_1^0}$ (black line), for the model PADM2M (Ziegler et al., 2011). The green line shows $\overline{g_1^0}$ for the last 780 kyr with a running average started following the most recent field reversal. Reversals indicated by vertical red lines. Note that PADM2M is derived from measurements of the squared field strength (Ziegler et al., 2011) and so the g_1^0 we determine from PADM2M must be bounded below by zero. g_1^0 does not go to zero when the field reverses due to uncertainties in timescales of the individual records combined to generate PADM2M and the smoothing applied in generating PADM2M via regularized inversion.

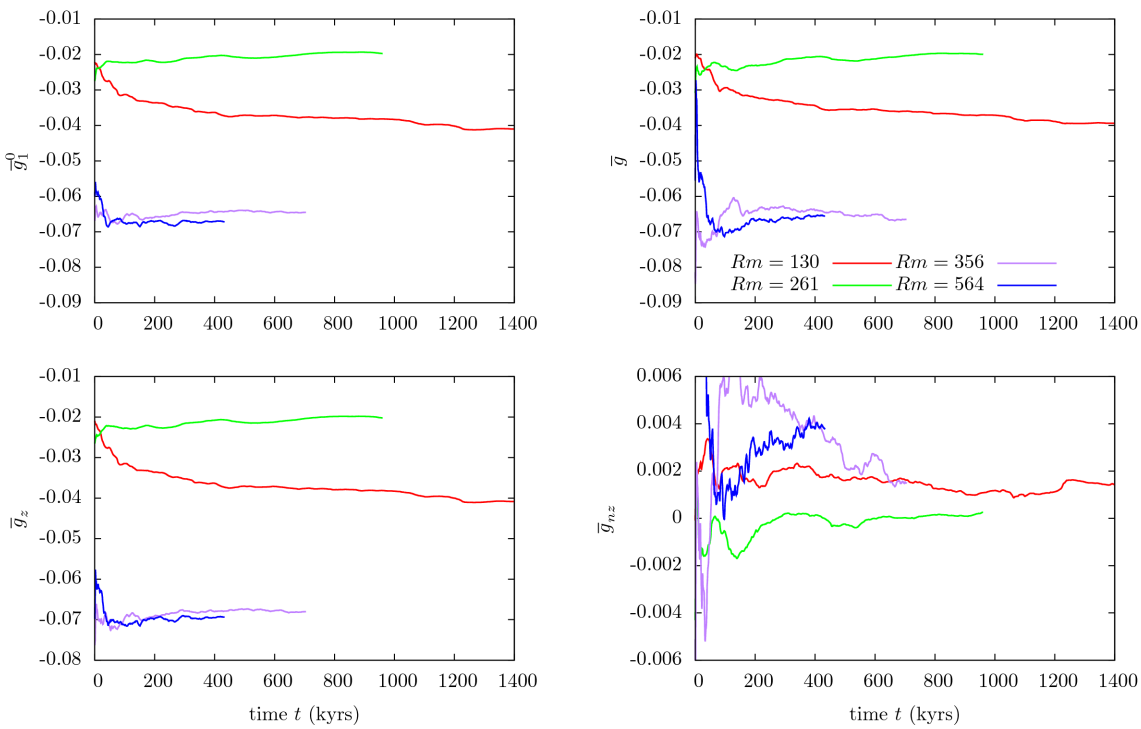

Figure 5: Running averages for the geodynamo simulations C4 ($Rm = 130$), C1-4 ($Rm = 261$), C8 ($Rm = 356$) and C10 ($Rm = 564$) in Table 1. Top left: the axial dipole coefficient, $\overline{g_1^0}$; top right: the sum of all coefficients, $\overline{g}$; bottom left: the sum of zonal ($m = 0$) coefficients, $\overline{g_z}$; bottom right: the sum of nonzonal ($m \neq 0$) coefficients, $\overline{g_{nz}}$. See text for details of model selection criteria.

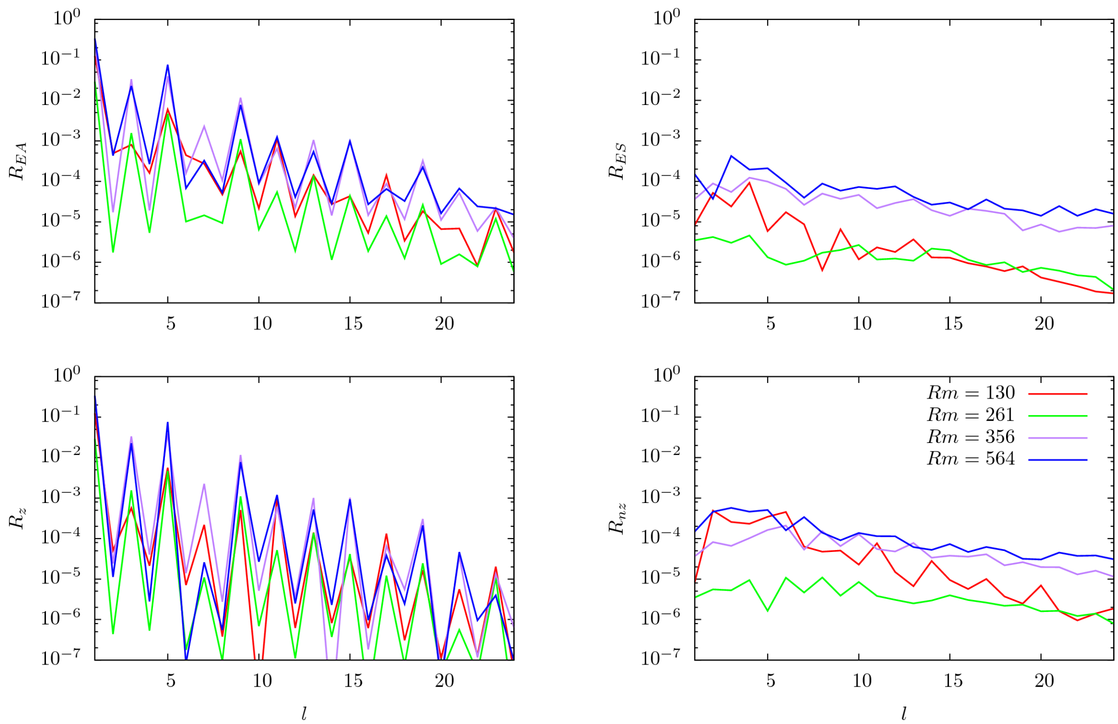

Figure 6: Components of the core surface power spectrum for the geodynamo simulations C4 ($Rm = 130$), C1-4 ($Rm = 261$), C8 ($Rm = 356$) and C10 ($Rm = 564$) in Table 1. Top left: equatorially antisymmetric ($l - m$ odd) power, R_{EA}; top right: equatorially symmetric ($l - m$ even) power, R_{ES}; bottom left: zonal ($m = 0$) power, R_z; bottom right: nonzonal ($m \neq 0$) power, R_{nz}. Gauss coefficients are averaged before calculating the spectra using (6) with the averaging time given in Table 1.

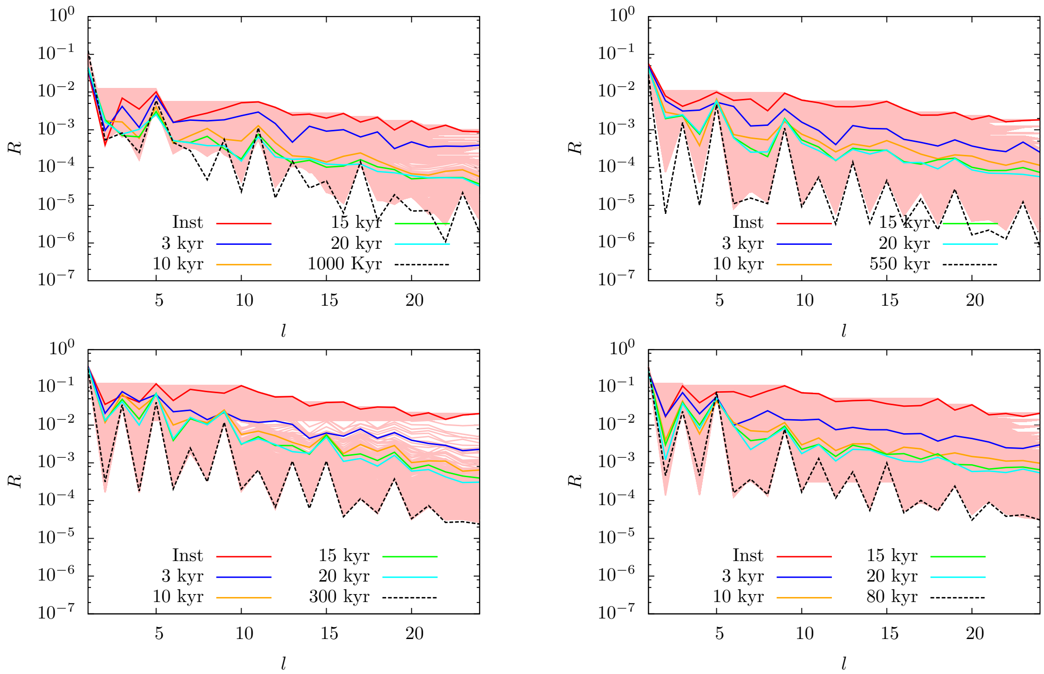

Figure 7: Core surface power spectra $R(l, r_o)$ averaged over increasing time periods (pink lines) with some averages highlighted. Models are C4 (Rm = 130, top left), C1-4 (Rm = 261, top right), C8 (Rm = 356, bottom left) and C10 (Rm = 564, bottom right).

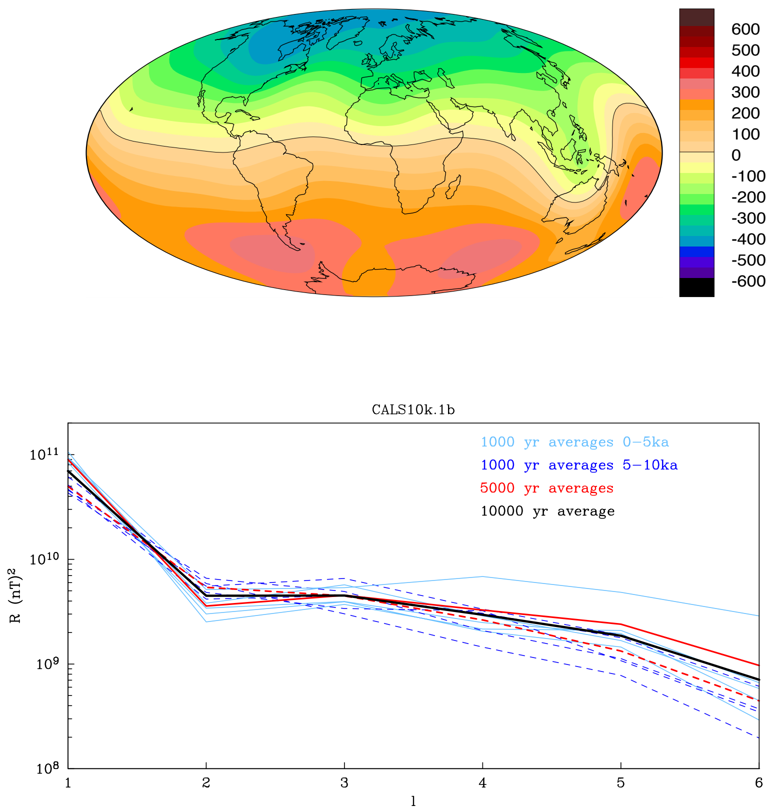

Figure 8: Radial component of the average magnetic field in μT at the CMB (top) and surface power spectra for different time-averages for the observational model CALS10K.1b (Korte et al., 2011). Dashed lines represent spectra from the early part of the model (5–10 ka) which has generally poorer spatial resolution.